agriculture

MDPI

*Article*

# Trait-Based Modeling of Surface Cooling Dynamics in Olive Fruit Using Thermal Imaging and Mixed-Effects Analysis

**Eddy Plasquy [1,*], José M. Garcia [2], Maria C. Florido [3] and Anneleen Verhasselt [4]**

[1] Center of Statistics, I_Biostat, Hasselt University, 3500 Hasselt, Belgium
[2] Department of Biochemistry and Molecular Biology of Plant Products (CSIC), Instituto de la Grasa, 41092 Seville, Spain; jmgarcia@ig.csic.es
[3] Department of Crystallography, Mineralogy and Agricultural Chemistry, Higher Technical School of Agronomic Engineering, University of Seville, 41013 Seville, Spain; florido@us.es
[4] Research Institute Center for Statistics (CENSTAT), Hasselt University, 3500 Hasselt, Belgium; anneleen.verhasselt@uhasselt.be
* Correspondence: eddy.plasquy@telenet.be

## Abstract

Effective postharvest cooling of olive fruit is increasingly critical under rising harvest temperatures driven by climate change. This study models passive cooling dynamics using a trait-based, mixed-effects statistical framework. Ten olive groups—representing seven cultivars and different ripening or size stages—were subjected to controlled cooling conditions. Surface temperature was recorded using infrared thermal imaging, and morphological and compositional traits were quantified. Temperature decay was modeled using Newton's Law of Cooling, extended with a quadratic time term to capture nonlinear trajse thectories. A linear mixed-effects model was fitted to log-transformed, normalized temperature data, incorporating trait-by-time interactions and hierarchical random effects. The results confirmed that fruit weight, specific surface area (SSA), and specific heat capacity (SHC) are key drivers of cooling rate variability, consistent with theoretical expectations, but quantified here using a trait-based statistical model applied to olive fruit. The quadratic model consistently outperformed standard exponential models, revealing dynamic effects of traits on temperature decline. Residual variation at the group level pointed to additional unmeasured structural influences. This study demonstrates that olive fruit cooling behavior can be effectively predicted using interpretable, trait-dependent models. The findings offer a quantitative basis for optimizing postharvest cooling protocols and are particularly relevant for maintaining quality under high-temperature harvest conditions.

**Keywords:** olive fruit; passive cooling; thermal imaging; mixed-effects model; postharvest handling

check for updates

Academic Editor: Perla A. Gómez

Received: 21 June 2025
Revised: 28 July 2025
Accepted: 29 July 2025
Published: 30 July 2025

**Citation:** Plasquy, E.; Garcia, J.M.; Florido, M.C.; Verhasselt, A. Trait-Based Modeling of Surface Cooling Dynamics in Olive Fruit Using Thermal Imaging and Mixed-Effects Analysis. *Agriculture* **2025**, *15*, 1647. https://doi.org/10.3390/agriculture15151647

## 1. Introduction

Olive production in the Mediterranean basin faces increasing challenges due to climate change. Rising harvest temperatures, reduced precipitation, and shifts in phenological cycles are disrupting the traditional timing and conditions of olive harvesting [1–4]. In southern Spain—one of the world's most productive olive-growing regions—harvest now often coincides with daytime temperatures exceeding 30 °C, especially for early-maturing cultivars like 'Arbequina' and 'Koroneiki'. Phenological shifts, including flowering occurring 17 days earlier, have been reported in response to regional warming, along with increased heat stress during reproductive stages [1,2]. Elevated temperatures during oil accumulation and harvest can significantly reduce fruit weight, oil concentration, and final oil quality. Cultivar-specific declines of up to 15% in oil content have been observed under high-temperature conditions in Koroneiki and other heat-sensitive cultivars [5,6].

Harvest temperature is a critical determinant of olive oil quality. When olives arrive at the mill with elevated internal temperatures, additional heat generated during crushing and malaxation can push fruit temperatures beyond thresholds known to trigger fermentation and sensory defects [7,8]. Moreover, high field temperatures during transport—especially in poorly ventilated containers—can accelerate anaerobic metabolism after just a few hours, leading to off-flavors and reduced commercial grades [9,10]. Although cold-pressing and thermal-control systems are increasingly employed, they often remain technically or economically unviable on a large scale [9]. These challenges underscore the urgent need for a deeper, fruit-specific understanding of postharvest cooling dynamics under realistic field conditions.

While internal temperature governs fruit quality, the current study focuses on the external cooling response, as measured by surface temperature decline under controlled convection conditions. Infrared thermography offers a non-invasive and high-resolution approach to capturing this dynamic, enabling empirical modeling of how fruit treatments influence early-stage thermal dissipation. Rather than simulating internal heat conduction, this study aims to generate trait-dependent biothermal data to inform temperature management protocols in postharvest systems.

The thermal response of olive fruit is influenced not only by ambient conditions but also by intrinsic fruit characteristics such as mass, geometry, moisture content, and internal composition. These factors affect both convective heat loss at the surface and conductive heat flow within the tissue [11,12]. Nevertheless, many fruit cooling models assume a constant rate of heat loss, overlooking cultivar- or maturity-related variation. Studies in apples have demonstrated genotype-dependent differences in cooling behavior related to surface exposure and airflow conditions, using energy-balance models and thermal imaging [13–15].

To analyze such variation, robust modeling tools are required. Linear mixed-effect models (LMMs) are particularly well-suited for modeling longitudinal, hierarchical data with repeated measurements [16,17]. When extended to include trait-by-time interactions and observation-level weights, these models can quantify how morphological and compositional traits affect cooling trajectories. Recent exploratory work on olive fruit has shown the feasibility of using LMMs to model surface cooling behavior [18]. The present study builds on that foundation with an expanded dataset and a more refined modeling framework, grounded in an extended (quadratic) form of Newton's Law of Cooling.

The aim of this study is to quantify how fruit-level morphological and compositional traits modulate surface cooling behavior in olive fruit, using thermal imaging and a trait-based mixed-effect modeling approach. While internal temperature ultimately determines quality outcomes, our focus here is to provide a surface-based thermal framework to support operational cooling decisions under elevated field temperatures.

## 2. Materials and Methods

### 2.1. Experimental Design and Sampling Strategy

The study was based on a laboratory-controlled cooling experiment designed to simulate rapid temperature drop in olive fruit postharvest. Data were collected over two seasons (2018–2019) at the Instituto de la Grasa (CSIC), Seville, Spain. Ten olive sample groups were analyzed, representing seven widely cultivated varieties in southern Spain. The sampling strategy also accounted for internal variation: three ripening stages of the

'Verdial' cultivar (unripe, medium, ripe) and two size-based categories of the 'Gordal' cultivar (small and large) were treated as separate groups.

Each sample group comprised 25 individual olives, resulting in a total of 250 fruits. This sampling frame allowed for exploration of both inter-varietal and intra-varietal cooling behavior, capturing morphological, developmental, and compositional diversity under uniform experimental conditions.

### 2.2. Biometric and Compositional Characterization

Each fruit was individually weighed to the nearest 0.01 g (DENVER Instrument APX-200) and measured for length and width using a digital caliper (resolution: 0.1 mm). Assuming a prolate spheroid shape, surface area (SA) and volume (V) were estimated using geometric formulae [19]:

$$SA = 2\pi b^2 + 2\pi / sin^{-1} e \quad (1)$$

$$V = \frac{4}{3}\pi a b^2 \quad (2)$$

where a is the semi-major axis (half-length), b the semi-minor axis (half-width), and $\boldsymbol{e} = \sqrt{1 - b^2/a^2}$ the eccentricity. Specific surface area (SSA) was then computed as SA divided by fruit mass (mm$^2$/g), yielding a mass-normalized proxy of external geometry and potential convective exchange efficiency.

To assess internal composition, all 25 olives per group were homogenized into a paste using a stainless-steel crusher. Moisture and oil content were determined by near-infrared spectroscopy (NIR; Foss 5000, wavelength range 1100–2500 nm). Oil content was reported both on a wet weight basis (CAH) and a dry weight basis (CAS). These values were then used to compute the water, oil, and solid fractions on a wet mass basis, following the approach detailed in Appendix A.2. Based on these fractions, the specific heat capacity (SHC, in J/kg·K) was estimated using a weighted average model:

$$\boldsymbol{C_p = w_{water} \cdot c_{water} + w_{oil} \cdot c_{oil} + w_{solids} \cdot c_{solids}} \quad (3)$$

where $\boldsymbol{c_{water}}$ = 4186, $\boldsymbol{c_{oil}}$ = 2000, and $\boldsymbol{c_{solids}}$ = 1400 J/kg·K. These values were derived from standard thermophysical data reported in the ASHRAE Handbook [18].

Although the pit was not modeled as a separate component, its thermal contribution was implicitly included by treating it as part of the residual solid fraction in the SHC calculation. Given that the specific heat of pit tissue is expected to be similar to that of other dry solids (approximately 1300–1500 J/kg·K), this simplification offers a reasonable approximation of the fruit's internal heat storage capacity. This approach maintains physical realism while avoiding unnecessary model complexity, given the focus on surface cooling behavior.

### 2.3. Thermal Imaging and Data Acquisition

Prior to cooling, olives were pre-heated to an internal temperature of approximately 39 ± 1 °C using a laboratory-grade heating chamber (BINDER FD720, 0.74 m$^3$). However, repeated opening of the incubator door and the time required for transfer introduced slight variability in initial temperature. As a result, starting surface temperatures ranged from 36 to 40 °C across samples.

Before imaging, the olives were arranged in a 5 × 5 notch grid on an insulated polyurethane tray. The tray was rapidly transferred into a freezing chamber maintained at −17 ± 1 °C. The chamber (volume ~50 m$^3$) provided uniform lateral airflow circulation, ensuring consistent cooling while avoiding direct air impingement on the samples.

Infrared thermal images were recorded using an FLIR Vue Pro 640 camera (Flir Systems, Inc., Wilsonville, OR, USA) (spectral range: 7.5–13.5 μm; resolution: 640 × 512 pix;

frame rate: 30 Hz; accuracy: ± 2°C). The camera was positioned 1 m above the tray and controlled remotely via MAVLink interface. Image capture was programmed at 10 s intervals over 5 to 12 min, depending on sample group, yielding 31 to 70 time points per fruit (see Appendix A for details).

Regions of interest (ROIs) were manually delineated around each fruit using FLIR Tools (v6.4), ensuring coverage of the central zone and minimizing edge artifacts. ROI resolution ranged from ~25 to >75 thermal pixels, reflecting differences in fruit size, orientation, and alignment. For each ROI at each time point, the mean surface temperature was extracted as the response variable. The pixel-level standard deviation (SD) was also recorded and used to estimate observation-level measurement variance.

### *2.4. Data Normalization and Thermodynamic Modeling*

To model fruit cooling, Newton's Law of Cooling was applied under the assumption of convective heat loss from the olive surface into a colder environment. This law is commonly used to describe unsteady heat transfer in biological systems where the Biot number (Bi) is low—i.e., when internal thermal resistance is small compared to external convective resistance. Under such conditions, the lumped capacitance approximation holds, and the fruit can be treated as thermally uniform throughout [20,21].

Given the small size of individual olive fruits, their relatively high thermal conductivity compared to the convective resistance at the surface, and the uniform airflow conditions of the experiment, a low Biot number was considered appropriate. Within this framework, surface temperature decay over fruit follows this expression:

$$T(t) = T_{ambient} + (T_0 - T_{ambient})e^{-kt} \tag{4}$$

where:

$T(t)$ is the surface temperature at time $t$;
$T_0$ is the initial fruit surface temperature at $t = 0$;
$T_{ambient}$ is the ambient temperature of the cooling chamber;
$k$ is the cooling rate constant (in $s^{-1}$);
$t$ is time (in seconds).

The linearized form suitable for estimation is

$$In[T(t) - T_{ambient}] = In(T_0 - T_{ambient}) - kt \tag{5}$$

To isolate the rate parameter and standardize starting conditions, temperature data were normalized:

$$log\left(\frac{T(t) - T_{env}}{T_0 - T_{env}}\right) = -kt \tag{6}$$

This transformation centers the decay curve to zero, ensuring that differences in initial temperatures do not bias slope estimates. However, exploratory plots revealed slight curvature in several log-transformed cooling trajectories, suggesting non-constant rates of cooling over time. To accommodate this, a quadratic extension was introduced:

$$log\left(\frac{T(t) - T_{env}}{T_0 - T_{env}}\right) = \beta_1 t + \beta_2 t^2 \tag{7}$$

Here:

$\beta_1$ represents the initial linear component of the cooling rate;
$\beta_2$ captures curvature or deceleration/acceleration in the cooling profile over time.

The initial cooling rate was estimated as $k_0 = -\beta_1$, corresponding to the instantaneous slope of the curve at $t = 0$, and was used for between-group comparisons.

Although classical heat transfer parameters such as heat flux, thermal resistance, and thermal conductivity were not directly measured, their influence was implicitly captured through trait-level predictors in the statistical modeling framework. Specifically, fruit weight, SSA, and SHC act as biophysical proxies that jointly determine the fruit's effective thermal exchange properties. These traits influence convective heat loss through their effects on thermal mass, surface area, and internal heat storage capacity, respectively. These traits, which are thus valid empirical stand-ins for underlying thermal processes under convective-based formulation, enable interpretable statistical modeling without relying on invasive or assumption-heavy internal measurements.

### 2.5. Statistical Modeling Framework

To model temperature decline over time, a linear mixed-effects model (LMM) was used with both fixed and random effects. The dependent variable was the normalized, log-transformed temperature for each fruit and time point. Fixed effects included time (linear and quadratic) and three continuous predictors: fruit weight, SHC, and residualized specific surface area (SSAresid). SSAresid refers to the residuals obtained by regressing SSA on weight and SHC; it captures the variation in specific surface area, which is independent of those two traits.

All continuous variables were z-standardized using the formula $z = (x - \overline{x})/s$, where $\overline{x}$ is the variable mean and $s$ is its standard deviation. Standardization facilitated the interpretability of effect sizes and improved model convergence. Interactions with time were specified for all continuous traits.

Categorical variables included pit shape (4 levels: narrow, medium, elongated, large–round) and flesh-to-stone ratio (3 levels: low, medium, high), which were entered as dummy-coded factors. Random intercepts were specified for both the olive groups (cultivar or developmental subgroup) to account for the hierarchical data structure.

To address observation-level variance due to differing pixel counts in the thermal ROIs, precision weights were defined as $w = 1/\left(SD^2 + \varepsilon\right)$, where SD is the pixel-based standard deviation, and $\varepsilon = 10^{-6}$ was added to ensure numerical stability.

Residuals were assumed to be independent and homoscedastic after weighting. Although autoregressive residual structures (AR (1)) were explored, they were not retained due to convergence issues. A diagnostic semi-variogram revealed no meaningful temporal autocorrelation, indicating that the inclusion of quadratic time terms sufficiently captured the serial structure.

The final model is expressed as

$$log\left(\frac{T_{ijk} - T_{env}}{T_{i0} - T_{en}}\right) = \beta_0 + \beta_1 t_k + \beta_2 t_k^2 + \sum_{m=1}^{M} \gamma_m X_{ijm} + \sum_{m=1}^{M} \theta_m X_{ijm} t_k + \delta_1^T FleshStone_{ij} + \delta_2^T PitShape_{ij} + u_j + v_{ij} + \epsilon_{ijk} \quad (8)$$

where

$\beta_0$: overall intercept;
$\beta_1$, $\beta_2$: fixed effects for linear and quadratic time terms;
$\gamma_m$: fixed effects for main effects of continuous predictors;
$\theta_m$: fixed effects for trait-by-time interactions;
$\delta_1^T$, $\delta_2^T$: transposed coefficient vectors for categorical traits;
$t_k$: time point(s);
$X_{ijm}$: standardized continuous predictors (weight, SHC, SSAresid);
$FleshStone_{ij}$, $PitShape_{ij}$: dummy-coded vectors for categorical traits;
$u_j \sim \mathcal{N}(0, \sigma_u^2)$: random intercept for group;

$v_{ij} \sim \mathcal{N}(0, \sigma_v^2)$: random intercept for fruit;
$\varepsilon_{ijk} \sim \mathcal{N}(0, \sigma^2)$: residual error.

The model was estimated using the lme () function from the lme4 package in R. Model performance was evaluated via marginal and conditional $R^2$, the Akaike Information Criterion (AIC), likelihood ratio tests (LRT), and residual diagnostics (Appendix A).

All data preprocessing, model implementation, and figure generation were conducted in R (version 4.4.3; R Core Team, 2025), using the lme4, nlme, tidyverse, and ggplot2 packages. ChatGPT (OpenAI GPT-4, 2025) contributed to refining the written presentation but not to statistical modeling or analytical decisions.

## 3. Results

### 3.1. Trait Variability and Thermal Data Overview

Olive fruit samples displayed substantial variability in both biometric and compositional traits across the ten cultivar groups. Table 1 summarizes group means and standard deviations for weight, surface area (SA), volume, specific surface area (SSA), and specific heat capacity (SHC). Fruit weight ranged from 1.50 g in 'Koroneiki' to 12.60 g in 'Gordal Big', with SSA inversely related to mass—exceeding 50 mm$^2$/g in small-fruited cultivars and falling below 20 mm$^2$/g in the largest. Moisture content spanned 47.2–58.4%, yielding SHC estimates between ~3140 and ~3780 J/kg·K (moisture data available in Appendix A Table A2).

**Table 1.** Biometric and compositional traits of olive fruit groups. Mean and standard deviation (SD) of weight (g), surface area (SA, mm$^2$), volume (V, mm$^3$), specific surface area (SSA, mm$^2$/g), and estimated specific heat capacity (SHC, J/kg·K) for each olive group (*n* = 25 per group).

| Olive Group | Weight | Surface | Volume | SSA | SHC |
|---|---|---|---|---|---|
| Arbequina | 2.38 ± 0.36 | 788.2 ± 80.4 | 2088.4 ± 325.5 | 332.2 ± 17.1 | 3299 ± 18 |
| Koroneiki | 1.50 ± 0.17 | 629.9 ± 52.1 | 1459.2 ± 182.2 | 421.2 ± 14.4 | 3129 ± 21 |
| Cacereña | 4.09 ± 0.51 | 958.1 ± 104.5 | 2760.7 ± 442.7 | 235.5 ± 12.9 | 3355 ± 17 |
| Hojiblanca | 5.68 ± 1.03 | 1490.4 ± 178.3 | 5375.2 ± 916.9 | 266.6 ± 19.9 | 3142 ± 21 |
| Picual | 4.42 ± 0.47 | 1261.4 ± 90.9 | 4153.9 ± 442.8 | 287.4 ± 13.1 | 3155 ± 21 |
| Verdial Unripe | 2.94 ± 0.41 | 1009.2 ± 97.6 | 2967.6 ± 435.6 | 344.2 ± 18.4 | 2880 ± 26 |
| Verdial Medium | 3.54 ± 0.38 | 1091.2 ± 77.4 | 3329.4 ± 351.1 | 310.3 ± 14.1 | 2911 ± 26 |
| Verdial Ripe | 5.40 ± 0.57 | 1440.7 ± 116.6 | 5070.4 ± 599.9 | 267.9 ± 12.4 | 2930 ± 26 |
| Gordal Small | 7.54 ± 1.24 | 1571.3 ± 180.8 | 5786.6 ± 980.6 | 210.3 ± 11.4 | 2950 ± 25 |
| Gordal Big | 12.60 ± 1.03 | 2317.3 ± 206.0 | 1026.0 ± 1383.0 | 184.0 ± 8.9 | 2852 ± 27 |

Thermal measurements were collected at high temporal resolution (31 to 70 time points per fruit), producing over 7500 observations. Figure 1 presents group-level mean cooling trajectories with 95% confidence intervals over the 360 s interval. All groups demonstrated monotonic decreases in surface temperature, but cooling rates and curve shapes differed markedly across cultivars and size classes. Arbequina, Picual, and Verdial Medium showed rapid declines, reaching temperatures below 10 °C by the end of the experiment. In contrast, Cacereña and Gordal Big retained higher temperatures throughout, indicating slower thermal dissipation and likely greater thermal inertia. These differences became more pronounced after the initial minute, suggesting that cultivar-specific traits such as fruit mass, surface-to-volume ratio, and internal composition influence both the initial cooling response and the longer-term temperature dynamics.

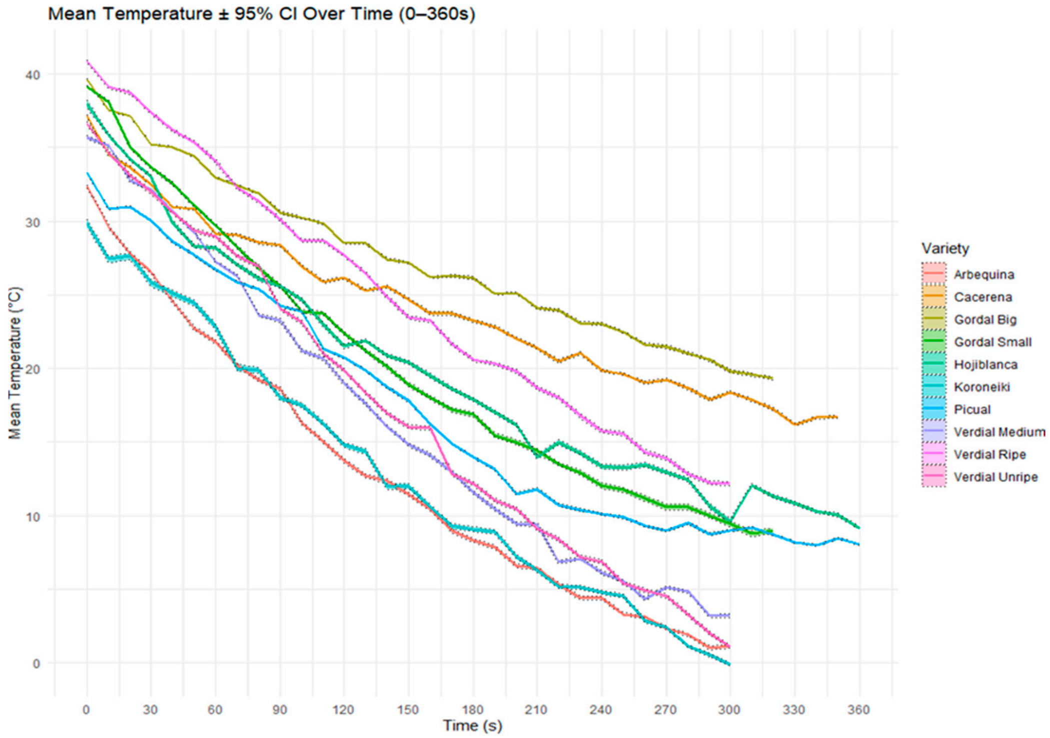

**Figure 1.** Average cooling curves per group with 95% CI (0–360 s). Mean surface temperature (°C) over time for each of the ten olive groups, recorded at 10 s intervals during passive cooling. Shaded bands represent pointwise 95% confidence intervals ($n$ = 25 fruits per group).

### 3.2. Preliminary Modeling and Empirical Behavior

Initial fits of Newtonian exponential models to normalized temperature trajectories yielded high $R^2$ values, typically above 0.90. However, residuals and visual inspection of log-transformed curves revealed slight but systematic curvature, suggesting that the cooling rate was not constant over time. To accommodate this behavior, a quadratic extension of the log–linear model was implemented:

$$log\left(\frac{T(t) - T_{env}}{T_0 - T_{env}}\right) = \beta_1 t + \beta_2 t^2 \tag{9}$$

Here, $T(t)$ is the fruit surface temperature at time $t$, $T_0$ is the initial temperature, and $T_{env}$ is the ambient temperature. Parameters $\beta_1$ and $\beta_2$ allow the cooling rate to vary over time. Differentiating Equation (9) with respect to time yields the instantaneous cooling rate:

$$k(t) = -\frac{d}{dt} log\left(\frac{T(t) - T_{env}}{T_0 - T_{env}}\right) = -(\beta_1 + 2\beta_2 t) \tag{10}$$

This formulation reveals that when $\beta_2 < 0$, the cooling process decelerates over time—as expected in larger fruits where internal conduction becomes limiting. Conversely, $\beta_2 > 0$ suggests initial resistance to heat loss followed by acceleration, possibly due to cuticular or surface effects. When $\beta_2 = 0$, the model reduces to the classical Newtonian form with a constant cooling rate $k(t) = -\beta_1$. In this special case, the temperature decline follows a pure exponential decay.

The initial cooling rate $t$ = 0, denoted as $k_0 = -\beta_1$, was retained as a comparative metric across groups. As shown in Figure 2, these initial rates varied substantially between cultivars.

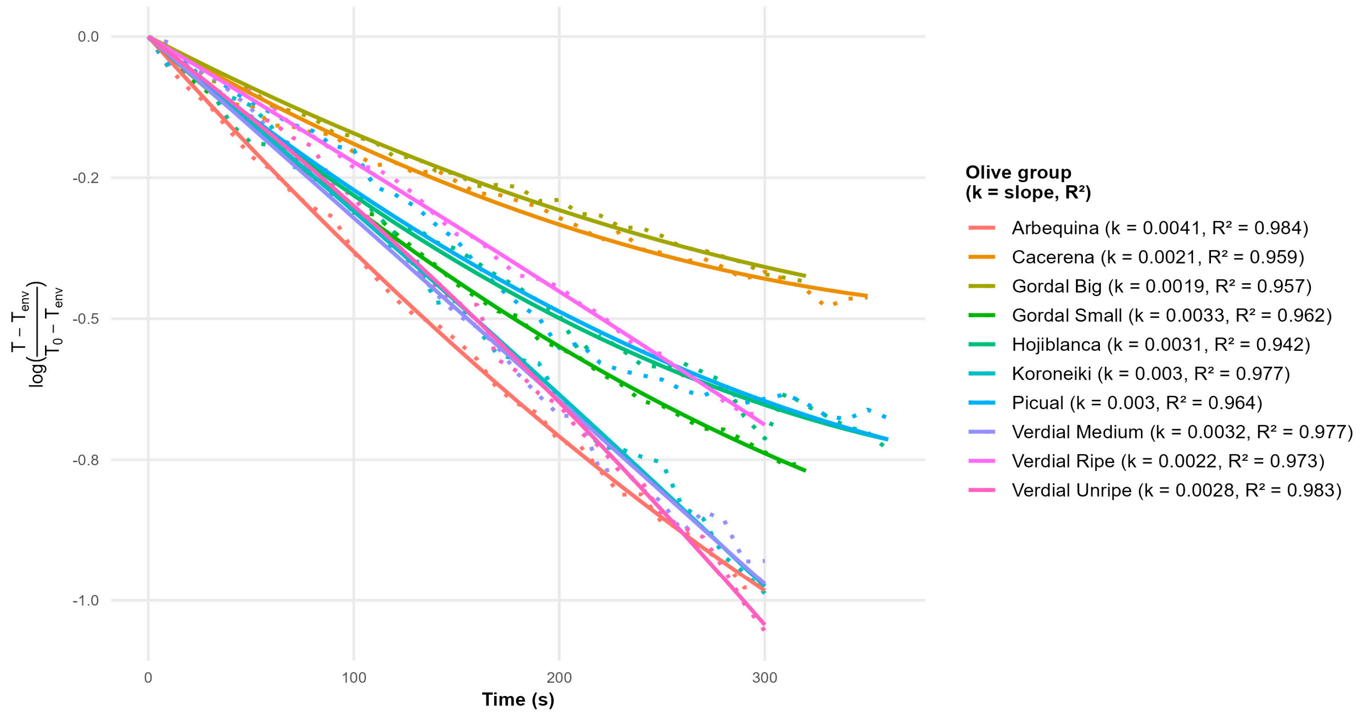

**Figure 2.** Normalized log–linear cooling curves (fruit-level means) fitted with exponential models. Each line represents the average cooling profile for an olive group, shown as the logarithm of the normalized temperature difference over time. Slopes correspond to cooling rate constants (k), with group-specific $R^2$ indicated. Dotted lines show empirical group means; solid lines are fitted exponential regressions.

Among the fastest-cooling groups were 'Koroneiki' and 'Verdial Unripe', while 'Gordal Big' and 'Cacereña' exhibited the slowest rates. These differences underscore the role of fruit-level characteristics beyond ambient conditions in modulating cooling behavior. Inclusion of the quadratic term $\beta_2 t^2$ allowed the model to capture subtle inflections in the log-temperature decay curves. High-SSA fruits exhibited steep early declines followed by stabilization, while larger, heavier fruits showed more gradual and persistent temperature loss. Thes patterns justify the inclusion of time-varying cooling effects and support the use of trait-by-time interaction in the fully developed LMM developed in Section 3.4.

Building on these findings, the next section explores the trait-level predictors of the variation in $k_0$ and extends the analysis to a multivariate context through principal component analysis (PCA).

### 3.3. Trait Associations with Cooling Rate

Univariate linear regressions showed that specific surface area (SSA) had the strongest negative association with $k_0$, explaining more than 50% of the variance ($R^2 = 0.512$). Fruit weight and SHC were also negatively associated with cooling rate but showed weaker correlations ($R^2 = 0.346$ and 0.056, respectively).

To explore the multivariate structure among traits, principal component analysis (PCA) was applied to standardized values of SSA, SHC, and weight. PC1 captured a size–efficiency gradient, with positive loadings for weight and negative loadings for SSA, reflecting a contrast between large, slow-cooling fruits and small, fast-cooling ones. PC2 was primarily driven by SHC, separating cultivars with higher internal energy storage capacity.

The PCA biplot (Figure 3) illustrates how cultivars are distributed in trait space and how these traits relate to cooling behavior. Fast-cooling groups cluster in the lower-left quadrant, characterized by high SSA and low SHC, while slow-cooling groups tend to occupy regions with higher weight and SHC. The directions and magnitudes of the red arrows indicate the relative contribution of each trait to the principal components.

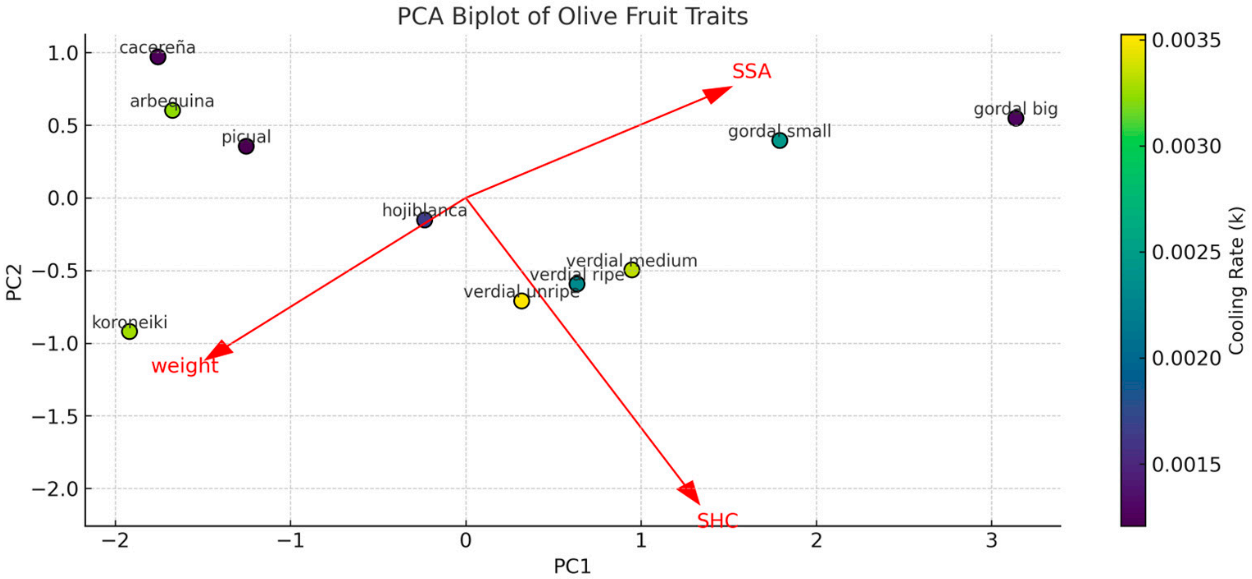

**Figure 3.** PCA biplot of fruit traits (weight, SHC, SSA) with cultivar positions and trait loadings. PC1 and PC2 were computed from standardized values of fruit weight, specific surface area (SSA), and specific heat capacity (SHC). Points represent olive group centroids, colored by initial cooling rate ($k_0$). Red arrows show trait loadings; their direction and length indicate each trait's contribution to the principal components. Groups with high SSA and low SHC cluster in regions associated with faster cooling.

A multiple linear regression of $k_0$ on PC1 and PC2 yielded an adjusted $R^2$ of 0.709, outperforming any individual trait model. This supports the conclusion that a combination of morphological and thermal traits jointly explains cooling variability more effectively than any individual trait. Table 2 summarizes the variance explained by each trait individually and in the PCA model.

**Table 2.** Variance explained ($R^2$) in initial cooling rate ($\mathbf{k_0}$) by single traits and PCA axes. Adjusted $R^2$ values for univariate regressions of $k_0$ on individual traits (SSA, weight, SHC) and for multivariate regression using the first two principal components (PC1 and PC2) derived from the trait structI removure.

| Predictor | $R^2$ |
|---|---|
| Specific Surface Area (SSA) | 0.512 |
| Weight | 0.346 |
| Specific Heat Capacity (SHC) | 0.056 |
| PCA (PC1 + PC2) | 0.709 |

Note: PCA model includes both PC1 and PC2 as predictors in a linear regression.

Other candidate traits—such as moisture content, pit size, and skin thickness—were considered during the exploratory analysis but were excluded from the final models. These traits were either highly collinear with the selected variables or showed limited explanatory power in univariate or PCA-based models. SSA, SHC, and weight were retained for their physical relevance, low collinearity, and mechanistic interpretability in relation to thermal exchange processes.

### *3.4. Mixed-Effects Model Results*

The linear mixed-effects model provided an excellent fit to the normalized log-transformed temperature trajectories. The fixed effects for time and time squared were highly significant ($p < 0.001$), confirming the nonlinear nature of the cooling process. All three continuous fruit-level traits—weight, specific heat capacity (SHC), and residualized specific surface area (SSAresid)—exhibited significant interactions with time (Table 3), indicating that their influence evolved dynamically over the course of cooling.

**Table 3.** Fixed-effect estimates from the final linear mixed-effects model (LMM). Estimates, standard errors (SE), and *p*-values for all fixed-effect terms in the final LMM, including main effects and time-by-trait interactions. Continuous predictors were standardized (mean = 0, SD = 1).

| Term | Estimate | Std. Error | *p*-Value |
|---|---|---|---|
| (Intercept) | 0.1907 | 0.1301 | 0.214 |
| Poly(time) | 0.005797 | $2.228 \times 10^{-5}$ | <0.001 |
| Poly(time$^2$) | $-6.882 \times 10^{-6}$ | $6.614 \times 10^{-8}$ | <0.001 |
| Weight_z | −0.001349 | 0.01104 | 0.901 |
| SHC_z | 0.06679 | 0.07582 | 0.425 |
| SSAresid_z | −0.01956 | 0.006275 | 0.002 |
| Flesh_stone | −0.04639 | 0.04842 | 0.4 |
| Pit_shape medium | −0.05286 | 0.1939 | 0.801 |
| Pit_shape elongated | −0.1177 | 0.2647 | 0.694 |
| Pit_shape large/round | −0.0396 | 0.3408 | 0.915 |
| Weight_z:time | −0.0007029 | $8.045 \times 10^{-6}$ | <0.001 |
| time:SHC_z | −0.0005999 | $8.453 \times 10^{-6}$ | <0.001 |
| time:SSAresid_z | $6.404 \times 10^{-5}$ | $6.972 \times 10^{-6}$ | <0.001 |

SSAresid exhibited a significant negative main effect ($p = 0.002$), suggesting that fruits with greater surface-to-mass ratios experienced faster baseline cooling. Its positive interaction with time indicates that the cooling rate in high-SSA fruits decreased more sharply over time, consistent with rapid initial heat loss followed by earlier stabilization. In contrast, while SHC and weight did not show significant main effects, both exhibited highly significant negative interactions with time ($p < 0.001$), indicating that higher SHC and heavier fruits slowed the rate of temperature decline, likely due to increased thermal inertia.

The model's marginal $R^2$ was 0.905, indicating that fixed effects alone explained over 90% of the variance in temperature response. The conditional $R^2$ rose to 0.984 when group- and fruit-level random effects were included, indicating excellent model performance at both fixed and hierarchical levels. Diagnostic checks—including residual plots and a semi-variogram (Appendix A), revealed no substantial heteroscedasticity or temporal autocorrelation, supporting the model's structural adequacy.

Figure 4 illustrates the predicted log-normalized temperature curves for low (−2 SD), mean, and high (+2 SD) values of each trait. High SSAresid values accelerated initial cooling but led to faster deceleration. Conversely, greater weight and SHC prolonged the cooling process, flattening the curve.

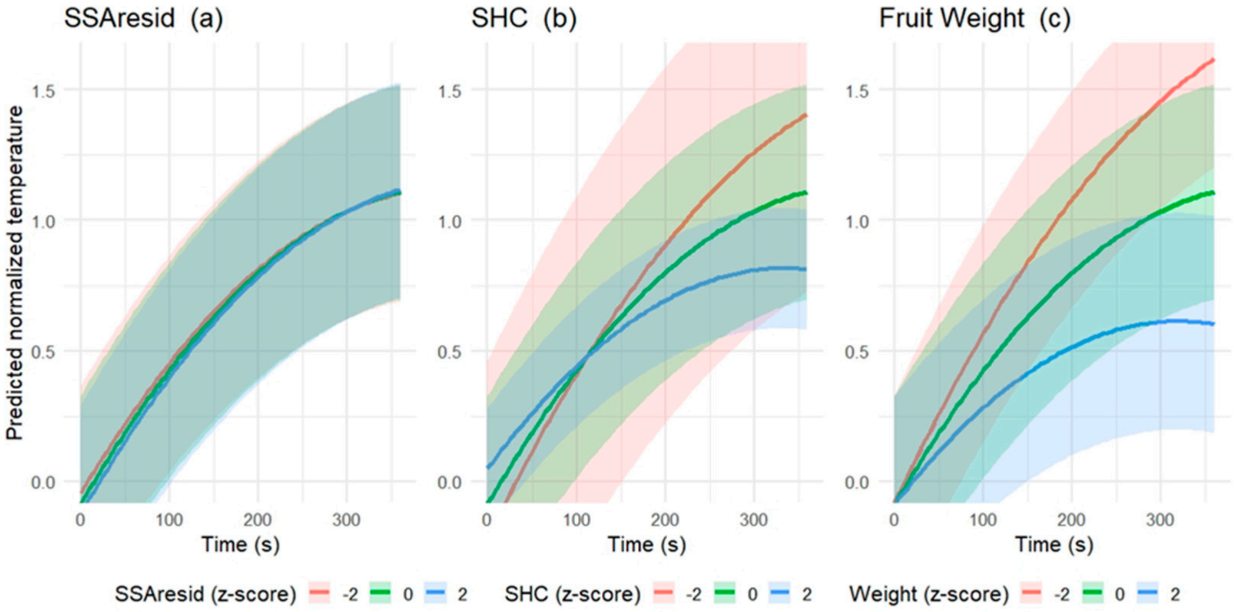

**Figure 4.** Predicted cooling trajectories by trait level with confidence intervals. Model-predicted log-transformed normalized temperature curves for low (−2 SD), average (0), and high (+2 SD) values of each continuous trait: (**a**) residualized specific surface area (SSAresid), (**b**) specific heat capacity (SHC), (**c**) fruit weight. Curves illustrate how trait variation alters the rate and curvature of cooling.

### *3.5. Derived Cooling Rates and Group-Level Effects*

The effective cooling rate $k_{eff}(t)$ was computed as the time derivative of the predicted log-normalized temperature trajectories:

$$k_{eff}(t) = -\frac{1}{T_{ijk} - T_{ambient}} \cdot \frac{dT}{dt} \tag{11}$$

Based on the model structure, by incorporating quadratic time and trait-by-time interactions into the model given in Equation (8), the full derivative becomes

$$\frac{dT}{dt} = \beta_1 + 2\beta_2 t + \sum_{m=1}^{M} \theta_m X_{ijm} \tag{12}$$

While $k_0 = -\beta_1$ serves as a convenient scalar summary of the initial cooling capacity, the effective cooling rate $k_{eff}(t)$ captures the dynamic, time-dependent nature of cooling. Traits such as SSAresid tend to accelerate early-stage cooling, while SHC and weight reduce the overall slope, consistent with higher thermal inertia. This distinction is particularly important in fruits exhibiting non-constant cooling behavior, where the rate of temperature change evolves due to their internal structure and composition.

Group-level predictions were generated by averaging the predicted log-normalized temperature curves within each cultivar group (Figure 5). Even after accounting for biometric traits, substantial between-group differences remained.

These group-specific deviations, captured by the random intercepts, highlight additional sources of anatomical or structural variation—such as pit architecture, cuticle thickness, or skin permeability—that were not directly modeled. While random effects do not influence the rate of temperature decline over time, they provide insight into cultivar-specific thermal profiles not explained by the measured predictors.

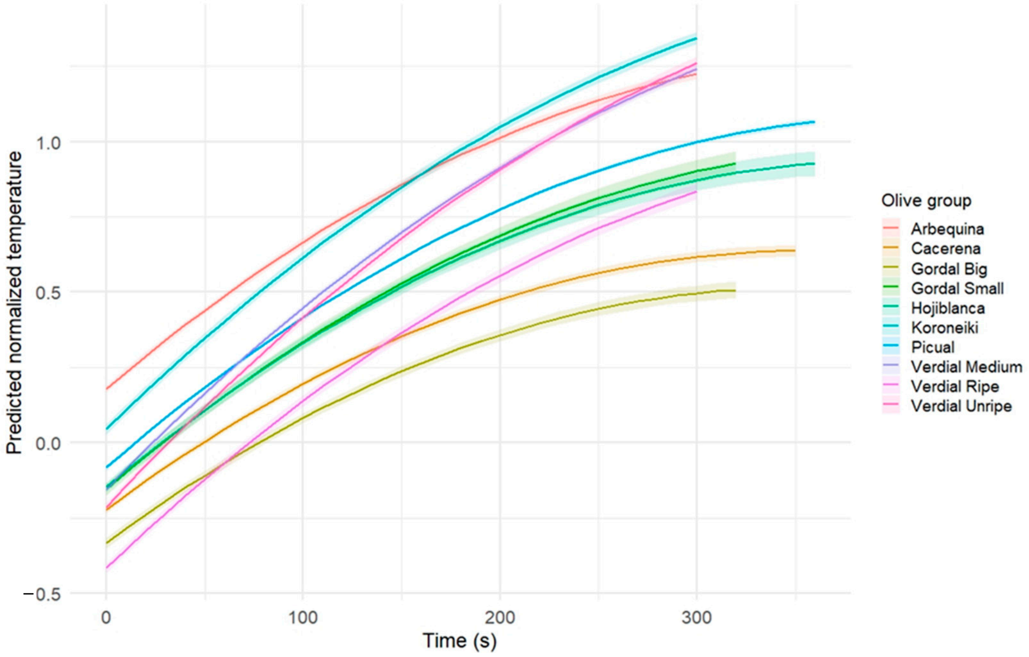

**Figure 5.** Predicted group-level cooling curves with confidence bands by olive group. Log-normalized temperature trajectories predicted by the final model for each group. Although the y-axis appears to rise, this reflects the diminishing temperature difference from ambient temperature as cooling progresses. The predictions incorporate both trait-based effects and group-level random intercepts.

### *3.6. Sensitivity Analysis and Model Robustness*

The contribution of each continuous fruit-level trait to model performance was assessed through nested model comparisons. For each trait—fruit weight, SHC, and SSAresid—a reduced model was fitted excluding the trait and its interaction with time. Likelihood ratio tests (LRTs) and changes in the Akaike Information Criterion (ΔAIC) were used to evaluate the impact of each exclusion.

Trait exclusion tests provided strong evidence for the independent contribution of each predictor. Removing weight led to a large drop in log-likelihood (LRT = 6297.8, df = 2, $p < 2.2 \times 10^{-16}$) and an AIC increase of 6257.1. Excluding SHC produced similarly strong effects (LRT = 3913.1; ΔAIC = 3882.2). While the magnitude was smaller, the removal of SSAresid still significantly impaired the model fit (LRT = 86.1; ΔAIC = 51.9).

To further evaluate robustness, the full model was re-estimated on 100 random subsamples (each 80% of the data). Across all iterations, the direction and magnitude of fixed-effect estimates remained consistent. Standard errors showed minimal inflation, and time-by-trait interactions retained statistical significance. These results suggest that the model’s outcomes are not overly dependent on any particular subset of the data.

Residual diagnostics showed no evidence of heteroscedasticity or serial correlation. Plots of standardized residuals versus fitted values displayed no systematic pattern. A semi-variogram of residuals, computed from within-fruit standardized errors, is presented in Figure 6. The absence of a rising trend across lags confirmed the assumption of residual independence.

Finally, an alternative covariance structure assuming autoregressive residuals (AR1) was tested using the nlme package. However, these models failed to converge due to singularity or rank deficiency. This instability is likely due to the short time series per fruit and the relatively low variability after accounting for fixed and random effects. Given the strong empirical support from residual diagnostics and the stability of the simpler model, we retained the assumption of independent residuals as a parsimonious and justifiable choice.

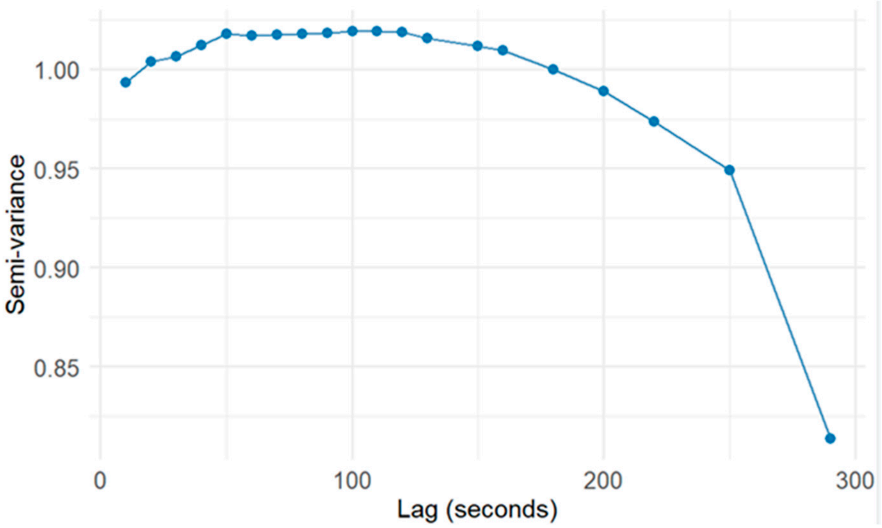

**Figure 6.** Semi-variogram of residuals within fruit. Semi-variance plotted against lag (seconds) across repeated measurements. The declining pattern confirms low temporal autocorrelation, validating the independence assumption used in the residual error structure.

Together, these analyses affirm the robustness and reliability of the trait-based linear mixed-effects model in capturing olive fruit cooling dynamics. The model's key conclusions—regarding the role of mass, surface geometry, and internal heat capacity—are statistically stable and resilient to data perturbations and alternative assumptions.

## 4. Discussion

### *4.1. Overview of Findings*

This study presents a detailed quantitative analysis of passive cooling in olive fruit under standardized postharvest conditions. High-resolution infrared thermal imaging and a comprehensive suite of morphological and compositional traits across ten olive groups were used to develop a trait-by-time modeling framework that characterizes surface temperature decline.

The application of a curve-level linear mixed-effects model enabled the integration of fixed and random effects, supporting dynamic, trait-dependent predictions of cooling behavior while accounting for the hierarchical structure of the data and observation-level variance. Among the continuous predictors, fruit weight, specific heat capacity (SHC), and residualized specific surface area (SSAresid) emerged as the most influential traits. Heavier fruits cooled more slowly due to increased thermal mass, while high SSAresid values accelerated heat dissipation through increased surface-to-mass ratios. SHC moderated cooling, with higher values associated with more gradual cooling, consistent with increased internal energy storage.

A major strength of the modeling approach lies in its ability to capture non-constant cooling rates via trait-by-time interaction terms. This represents a significant advancement over conventional Newtonian cooling models with fixed decay rates. The resulting trait-specific cooling profiles are not only statistically robust but also mechanistically interpretable, reflecting the interplay between surface exposure, internal conduction, and compositional traits. This biologically informed representation of postharvest thermal behavior provides both theoretical insight and practical guidance for fruit handling under variable thermal conditions.

The observed curvature in temperature decline, particularly the deceleration of cooling in heavier fruits and early stabilization in small high-SSA fruits, aligns with the unsteady-state heat transfer theory. While this general pattern is well known in physical modeling, the present study contributes to the literature by formally capturing these dynamics through a statistically rigorous, trait-based framework. By extending Newton's Law of Cooling with a quadratic time component and incorporating trait interactions, the model links measurable fruit characteristics to temporal cooling trajectories. This structure enables cultivar-specific, trait-sensitive predictions of cooling behavior in real-world conditions.

Although research on surface cooling dynamics in olives is limited, analogous thermophysical patterns have been reported in apples and other fruits, where factors such as skin conductance, airflow exposure, and internal composition affect heat loss [13,14]. The findings of this study contribute to this growing body of literature while offering a novel statistical approach tailored to olive fruit.

### *4.2. Methodological Contributions and Limitations*

The modeling strategy employed in this study builds on and extends prior exploratory work by incorporating fruit traits into a mixed-effects framework, thereby linking physiological attributes to thermal behavior. The use of a quadratic log–linear model enabled more accurate representation of empirical cooling curves compared to classical Newtonian or segmented alternatives—particularly for fruits exhibiting structural heterogeneity or non-uniform thermal response.

Several methodological features contributed to the robustness of the model. First, observation-level precision weights, derived from pixel-level temperature variance, ensured that higher-variance observations exerted less influence on parameter estimation, thereby reducing noise. Second, diagnostic analysis—including residual plots and a semivariogram—supported the assumption of independent residuals, validating the model structure in the absence of autocorrelation. Third, the inclusion of random intercepts at both the fruit and group levels effectively captured unobserved heterogeneity related to cultivar-specific traits such as pit architecture, skin permeability, or internal porosity.

Nonetheless, this study has several limitations. The experiment was conducted within a single, highly controlled thermal environment, which may not fully replicate the thermal variability experienced during commercial harvest, transport, and storage. The relative short cooling duration ($\leq$12 min) may also limit the detection of slower, long-term conductive effects, particularly in larger fruits.

Additionally, some potentially important anatomical and compositional traits—such as wax layer thickness, surface roughness, or tissue density—were not measured and could further refine trait-based predictions if included in future studies. While the study design included three ripening stages for Verdial and two size-based classes for Gordal, other cultivars were not assessed across multiple phenological stages. This imbalance limits the ability to generalize findings about developmental trends across all varieties.

Finally, although surface temperature was used as a practical and non-invasive proxy for the thermal state, it does not capture internal temperature gradients or the full extent of intra-fruit heat conduction. Incorporating internal temperature measurements or developing multi-zone heat transfer models could provide more complete insight into fruit thermal dynamics, particularly in applications where core temperature critically affects product quality or safety.

Despite these limitations, the modeling framework developed in this study remains broadly applicable and can serve as a foundation for further research on postharvest thermal behavior in horticultural products.

### *4.3. Applications and Future Directions*

The trait-based findings of this study offer practical value for optimizing postharvest cooling protocols in olive production systems. By identifying cultivar and developmental groups with slower cooling responses, producers and facility operators can adapt precooling durations, regulate airflow intensity, or modify storage configurations to enhance temperature uniformity across harvested batches.

The analytically derived effective cooling rate, $k_{eff}(t)$, provides a dynamic and interpretable proxy for thermal exchange capacity. This time-resolved rate function can support the calibration of cooling infrastructure and the tailoring of handling strategies to cultivar-specific thermal behavior. Recent advancements in pilot-scale thermal conditioning systems have demonstrated potential for industrial implementation [10,22,23]. However, such systems typically operate without trait-based customization. The results of this study suggest that incorporating measurable fruit traits into the control logic of cooling systems could significantly enhance efficiency and product quality preservation.

Although this study focused on continuous cooling trajectories, an important direction for future research involves modeling time-to-threshold outcomes—such as the time required for surface or core temperature to fall below a defined threshold. Framing the problem within a survival analysis context would enable more flexible and informative comparisons of cultivar resilience under varying thermal loads. A forthcoming study will explore this approach, using event-time modeling to quantify differences in cooling performance across groups and trait profiles.

### *4.4. Societal Relevance and Ethical Considerations*

This research contributes to the broader effort of developing climate-resilient postharvest systems for Mediterranean agriculture. Rising harvest temperatures pose a growing threat to fruit quality, oil stability, and economic returns—especially for cultivars harvested at early maturity or subjected to mechanical handling. By providing a mechanistic, trait-based understanding of olive fruit cooling, this study supports the transition toward precision strategies in thermal management.

The modeling approach emphasizes both transparency and reproducibility. Rather than relying on opaque, data-driven algorithms, the study adopts a physically grounded statistical framework that enables direct interpretation of model parameters in terms of fruit morphology and thermophysical properties. This facilitates collaboration between agronomists, engineers, and postharvest specialists and promotes integration of the findings into practical applications.

From an ethical perspective, improving cooling strategies aligns with the imperative to reduce postharvest losses, conserve resources, and support sustainable agriculture. Such improvements are particularly relevant for small-scale producers and cooperatives, which often operate under economic and logistical constraints.

By enabling trait-informed handling strategies, the outcomes of this study contribute to a more adaptive and equitable agricultural value chain. Future implementation of trait-based cooling protocols could help mitigate climate-related risks while ensuring consistent product quality across diverse growing regions and market conditions.

## 5. Conclusions

This study presents a comprehensive, trait-based analysis of passive cooling behavior in olive fruit under controlled laboratory conditions. By integrating thermal imaging, detailed morphological profiling, and a hierarchical mixed-effects modeling framework, the research demonstrates how measurable fruit-level traits govern both the rate and shape of postharvest temperature decline.

The key findings emphasize the dominant role of fruit mass, specific surface area (SSA), and specific heat capacity (SHC) in shaping cooling dynamics. Importantly, these effects were shown to be time-dependent, with trait-by-time interactions capturing the evolving nature of thermal exchange. The quadratic extension of Newton's Law of Cooling proved essential in accounting for the observed curvature in the cooling trajectories, thereby enabling the derivation of a dynamic, interpretable effective cooling rate.

The proposed modeling approach is statistically robust, physically interpretable, and extensible to other fruit systems. Its performance was validated through residual diagnostics, nested model comparisons, and subsampling-based sensitivity analyses. The inclusion of pixel-level measurement variance and random effects enhanced both precision and generalizability.

From an applied perspective, this study provides actionable insights for optimizing postharvest cooling protocols. Traits associated with faster or slower cooling behavior can inform cultivar-specific decisions regarding pre-cooling time, airflow regulation, and storage design. These recommendations are particularly salient in the context of climate change, where elevated field temperatures and extended harvest seasons increase the risk of thermal damage and quality loss.

In summary, the trait-based linear mixed-effects model developed in this study offers a data-informed framework for understanding and predicting cooling behavior in olive fruit. The approach bridges physical theory with empirical modeling and lays the groundwork for future research into internal heat conduction, time-to-threshold performance, and operational integration in commercial cooling systems. As climate pressures intensify, such trait-informed strategies may prove essential in supporting resilient and high-quality postharvest supply chains.

**Author Contributions:** Conceptualization, E.P.; methodology, E.P. and A.V.; software, E.P.; validation, E.P., J.M.G. and A.V.; formal analysis, E.P., M.C.F. and A.V.; investigation, E.P. and J.M.G.; resources, E.P. and J.M.G.; data curation, E.P. and M.C.F.; writing—original draft preparation, E.P.; writing—review and editing, J.M.G., M.C.F. and A.V.; visualization, E.P.; supervision, A.V.; project administration, E.P. All authors have read and agreed to the published version of the manuscript.

**Funding:** This research received no external funding.

**Data Availability Statement:** The original contributions presented in this study are included in the article. Further inquiries can be directed to the corresponding author.

**Acknowledgments:** During the preparation of this manuscript, the authors used ChatGPT [OpenAI GPT-4, 2025] for the purposes of refining the written presentation but not for statistical modeling or analytical decisions. The authors have reviewed and edited the output and take full responsibility for the content of this publication.

**Conflicts of Interest:** The authors declare no conflicts of interest.

## Appendix A

### *Appendix A.1. Pixel Count Overview and Sample Times*

This appendix provides a detailed overview of the thermal imaging structure used in the cooling experiment. Table A1 summarizes the number of thermal pixels captured per observation (per fruit per time point) and the total number of time points acquired for each of the ten olive groups. These data reflect both biological and technical variability, including differences in fruit size, shape, orientation, and manual region-of-interest (ROI) delineation.

Most varieties were monitored for 300 s (31 time points at 10 s intervals). However, three groups were recorded over longer durations—Cacereña, 36 time points (350 s); Picual, 61 time points (600 s); Hojiblanca, 70 time points (700 s)—though one measurement (at 270 s) was missing. The table below reports the total number of temperature observations and the average number of thermal pixels per fruit ROI across the cooling series.

**Table A1.** Biothermal data.

| Olive Group | Olives (*n*) | # Points | Time Range | Mean Pixels Per ROI |
|---|---|---|---|---|
| Arbequina | 25 | 31 | 300 s (5 min) | 39.97 |
| Koroneiki | 25 | 31 | 300 s (5 min) | 48.53 |
| Cacereña | 25 | 36 | 350 s (5 min 50 s) | 54.38 |
| Hojiblanca | 25 | 70 * | 700 s (11 min 40 s) | 88.81 |
| Picual | 25 | 61 | 600 s (10 min) | 100.97 |
| Verdial Unripe | 25 | 31 | 300 s (5 min) | 74.28 |
| Verdial Medium | 25 | 31 | 300 s (5 min) | 47.28 |
| Verdial Ripe | 25 | 31 | 300 s (5 min) | 47.17 |
| Gordal Small | 25 | 33 | 320 s (5 min 20 s) | 50.33 |
| Gordal Big | 25 | 33 | 320 s (5 min 20 s) | 50.33 |

* Hojiblanca contains a missing time point at 270 s.

A heatmap of pixel counts per fruit and time point is presented in Figure A1. The variation in region-of-interest (ROI) resolution—ranging from ~25 to over 75 pixels—illustrates both biological and technical heterogeneity. This justifies the use of observation-level precision weights in the statistical model, ensuring that measurements with lower pixel counts exert proportionally less influence on fixed-effect estimation.

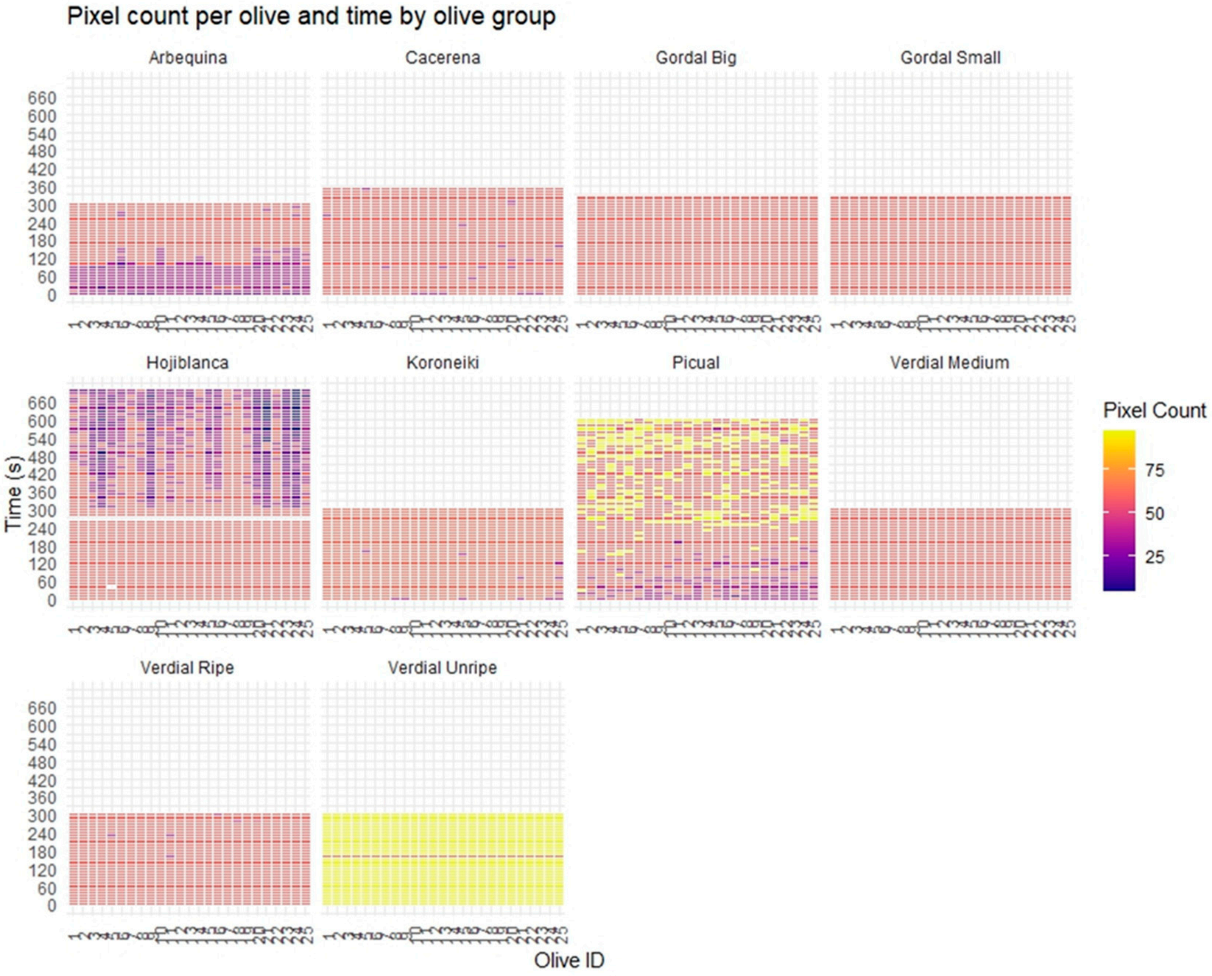

**Figure A1.** Heatmap of pixel counts per fruit and time point. ROI-based pixel counts for each olive across time, stratified by group. Rows indicate time (in seconds), and columns represent individual olives. Color scale reflects pixel density, from low (purple) to high (yellow). Differences in pixel resolution reflect fruit size, ROI delineation, and image alignment.

### *Appendix A.2. Biochemical Composition and SHC Estimates*

To ensure a physically consistent estimation of specific heat capacity (SHC) for each olive group, component fractions of water, oil, and residual solids were first converted to a wet mass basis. The method proceeds as follows:

Water fraction was derived from moisture content, expressed as a percentage of fresh weight:

$$\boldsymbol{w_{water}} = \frac{\boldsymbol{Moisture}\ (\%)}{\mathbf{100}} \tag{A1}$$

The oil fraction was available as follows: CAH, percentage of wet weight, and CAS, percentage of dry weight. To align CAS with the wet-basis mass balance, it was adjusted according to the dry matter fraction:

$$\boldsymbol{w_{oil}} = (\mathbf{1} - \boldsymbol{w_{water}})\cdot\frac{\boldsymbol{CAS}}{\mathbf{100}} \tag{A2}$$

The remaining mass was attributed to non-oil solids:

$$w_{solids} = (1 - w_{water}) - w_{oil} \tag{A3}$$

SHC was then estimated using a weighted average of the specific heat capacities of the three components:

$$C_p = w_{water}\cdot c_{water} + w_{oil}\cdot c_{oil} + w_{solids}\cdot c_{solids} \tag{A4}$$

where

$c_{water}$ = 4186 J/kg·K;
$c_{oil}$ = 2000 J/kg·K (mean value from the 1900–2100 range);
$c_{solids}$ = 1400 J/kg·K (mean value from the 1300–1500 range).

To reflect the uncertainty in the oil and solid heat capacity values, minimum and maximum estimates were calculated using the extremes of their respective ranges. These were used to derive an approximate standard deviation for SHC in each group:

$$SD\left(C_p\right) = \frac{C_p^{max} - C_p^{min}}{4} \tag{A5}$$

**Table A2.** Moisture, oil content, and SHC (mean ± SD) by olive group.

| Olive Group | CAH (%) | CAS (%) | Moister (%) | Specific Heat (±SD) |
|---|---|---|---|---|
| Arbequina | 16.70 | 47.15 | 64.58 | 3299.40 ± 17.71 |
| Koroneiki | 19.22 | 45.69 | 57.93 | 3129.26 ± 21.03 |
| Cacereña * | 16.15 | 47.31 | 66.80 | 3355.29 ± 16.60 |
| Hojiblanca | 17.53 | 42.50 | 58.76 | 3142.21 ± 20.62 |
| Picual | 21.79 | 52.19 | 58.31 | 3155.06 ± 20.84 |
| Verdial Unripe | 25.82 | 52.65 | 47.15 | 2880.55 ± 26.42 |
| Verdial Medium ** | 27.29 | 56.43 | 47.91 | 2911.14 ± 26.04 |
| Verdial Ripe | 28.76 | 56.43 | 48.67 | 2929.74 ± 25.66 |
| Gordal Small | 27.85 | 52.16 | 50.04 | 2950.47 ± 24.98 |
| Gordal Big | 26.30 | 47.23 | 46.71 | 2852.35 ± 26.64 |

* Data retrieved from [24]; ** mean of Verdial Unripe and Medium.

### *Appendix A.3. Variance Inflation Factors (VIFs)*

To assess multicollinearity among predictors in the final model, variance inflation factors (VIFs) were computed. The analysis included all continuous variables and interactions considered during model building.

Prior to model fitting, volume and surface area were excluded due to extreme collinearity with weight (VIF > 150) and SSA, respectively. Additionally, SSA was residualized against log-weight to create SSAresid, reducing collinearity while preserving independent geometric information.

The table below summarizes the VIFs for the final set of continuous predictors and their interaction terms. All values remained well below the commonly used threshold of 5, indicating that multicollinearity was not a major concern in the final model.

**Table A3.** Variance inflation factors for continuous predictors (mean effects and interactions).

| **Predictor** | **VIF** |
|---|---|
| Weight | 1.72 |
| SHC | 1.39 |
| SSAresid | 1.58 |
| Weight × time | 1.75 |
| SHC × time | 1.41 |
| SSAresid × time | 1.66 |

Note: VIFs were computed using the car:vif () function after fitting an equivalent linear model with the same structure (excluding random effects).

### *Appendix A.4. Likelihood Ratio Tests for Model Sensitivity*

To evaluate the individual contribution of each continuous trait to the model's explanatory power, nested model comparisons were performed using likelihood ratio tests (LRTs). For each trait, a reduced model was constructed by removing the main effect and its interaction with time from the full model. These reduced models were then compared to the full model using maximum likelihood estimation.

**Table A4.** Likelihood ratio tests for the exclusion of continuous traits.

| **Predictor Removed** | **Δ Log-Likelihood** | **DF** | **LRT *p*-Value** | **ΔAIC** |
|---|---|---|---|---|
| Weight | 6297.8 | 2 | $<2.2 \times 10^{-16}$ | +6257.1 |
| SHC | 3913.1 | 2 | $<2.2 \times 10^{-16}$ | +3882.2 |
| SSAresid | 86.1 | 2 | $<2.2 \times 10^{-16}$ | +51.9 |

Each trait—weight, SHC, and SSAresid—significantly contributed to the model's ability to explain the variability in cooling trajectories. The largest LRT statistics were associated with weight and SHC, suggesting their strong independent effects on the temperature decay pattern. While the effect of SSAresid was smaller, its exclusion still resulted in a significant deterioration in model fit.

These findings confirm that all three continuous predictors are essential to the explanatory structure of the final model.

## References

1. Gabaldón-Leal, C.; Ruiz-Ramos, M.; De La Rosa, R.; León, L.; Belaj, A.; Rodríguez, A.; Santos, C.; Lorite, I.J. Impact of Changes in Mean and Extreme Temperatures Caused by Climate Change on Olive Flowering in Southern Spain. *Int. J. Climatol.* **2017**, *37*, 940–957. [CrossRef]
2. García-Mozo, H.; Oteros, J.; Galán, C. Phenological Changes in Olive (*Olea europaea* L.) Reproductive Cycle in Southern Spain Due to Climate Change. *Ann. Agric. Environ. Med.* **2015**, *22*, 421–428. [CrossRef] [PubMed]

3. Fraga, H.; Pinto, J.G.; Santos, J.A. Climate Change Projections for Chilling and Heat Forcing Conditions in European Vineyards and Olive Orchards: A Multi-Model Assessment. *Clim. Change* **2019**, *152*, 179–193. [CrossRef]
4. Mihailescu, E.; Soares, M.B. The Influence of Climate on Agricultural Decisions for Three European Crops: A Systematic Review. *Front. Sustain. Food Syst.* **2020**, *4*, 64. [CrossRef]
5. Nissim, Y.; Schwartz, A.; Peer, R.; Dag, A.; Zipori, I.; Erel, R. High Temperature during Oil Accumulation Decreased Oil Yield and Quality in 'Koroneiki' Olive Trees. *PLoS ONE* **2020**, *15*, e0231314. [CrossRef] [PubMed]
6. Mousavi, S.; Taghvaei, M.; Bakhshi, D.; Khadivi-Khub, A.; Shirazi, M.; Karimi, M.; El-Mashad, H.M. Temperature Stress Alters Fruit Development and Oil Characteristics in Three Olive Cultivars under Field Conditions. *Agronomy* **2022**, *12*, 227. [CrossRef]
7. Angerosa, F.; Mostallino, R.; Basti, C.; Vito, R. Effect of Malaxation Temperature on the Virgin Olive Oil Phenolic Profile under Laboratory-Scale Conditions. *Eur. J. Lipid Sci. Technol.* **2001**, *103*, 228–234.
8. Kalua, C.M.; Bedgood, D.R., Jr.; Bishop, A.G.; Prenzler, P.D. Changes in Volatile and Phenolic Compounds with Malaxation Time and Temperature during Virgin Olive Oil Production. *J. Agric. Food Chem.* **2006**, *54*, 7641–7651. [CrossRef] [PubMed]
9. Mayo, R.; Altisent, R.; Moyano, M.; Gavara, R.; Rijk, R. Cold Storage and Temperature Management of Olive Fruit. *Processes* **2021**, *9*, 1543. [CrossRef]
10. Plasquy, E.; Florido, M.C.; Sola-Guirado, R.R.; García Martos, J.M.; García Martín, J.F. Effect of Temperature and Time on Oxygen Consumption by Olive Fruit: Empirical Study and Simulation in a Non-Ventilated Container. *Fermentation* **2021**, *7*, 200. [CrossRef]
11. Plasquy, E.; García, J.M.; Florido, M.C.; Sola-Guirado, R.R. Estimation of the Cooling Rate of Six Olive Cultivars Using Thermal Imaging. *Agriculture* **2021**, *11*, 164. [CrossRef]
12. Gowen, A.; Tiwari, B.; Cullen, P.; McDonnell, K.; O'Donnell, C. Applications of Thermal Imaging in Food Quality and Safety Assessment. *Trends Food Sci. Technol.* **2010**, *21*, 190–200. [CrossRef]
13. Saudreau, O.; Cormier, L.; Casenave, A.; Stoll, M.; Gibon, J.; Le Goff, C. Modeling Apple Surface Temperature with Energy-Balance and Infrared Thermography: A Field-Based Approach. *Biosyst. Eng.* **2015**, *139*, 20–32.
14. Tsoulias, N.; Jörissen, S.; Nüchter, A. An approach for monitoring temperature on fruit surface by means of thermal point cloud. *MethodsX* **2022**, *9*, 101712. [CrossRef] [PubMed]
15. Verbeke, G.; Molenberghs, G. *Linear Mixed Models for Longitudinal Data*; Springer: New York, NY, USA, 2000.
16. Zeger, S.L.; Liang, K.Y. Longitudinal Data Analysis for Discrete and Continuous Outcomes. *Biometrics* **1986**, *42*, 121–130. [CrossRef] [PubMed]
17. ASHRAE. Methods of Precooling Fruits and Vegetables. In *ASHRAE Handbook—Refrigeration*; American Society of Heating, Refrigeration and Air-Conditioning Engineers (ASHRAE): Peachtree Corners, GA, USA, 2006; Chapter 9.
18. Thibodeau, B.A.; Bhandari, B.R.; Truong, V.D. Modeling Surface Area and Volume of Ellipsoidal Agricultural Products. *J. Food Eng.* **2000**, *45*, 87–94.
19. Incropera, F.P.; DeWitt, D.P.; Bergman, T.L.; Lavine, A.S. *Fundamentals of Heat and Mass Transfer*, 6th ed.; Wiley: Hoboken, NJ, USA, 2007.
20. Çengel, Y.A. *Heat and Mass Transfer: A Practical Approach*, 4th ed.; McGraw-Hill: New York, NY, USA, 2008.
21. Plasquy, E.; García Martos, J.M.; Florido Fernández, M.C.; Sola-Guirado, R.R.; García Martín, J.F. Adjustment of Olive Fruit Temperature before Grinding for Olive Oil Extraction: Experimental Study and Pilot Plant Trials. *Processes* **2021**, *9*, 586. [CrossRef]
22. Calatayud, M.; Vendrell, M.; Brizzolara, S.; Meoni, G.; Tenori, L.; Luchinat, C.; Tonutti, P. Effects of Pre-Processing Cooling Treatments of Harvested Olives on Oil Volatilome and Quality Parameters. *Acta Hortic.* **2023**, *1364*, 127–134. [CrossRef]
23. Kleinbaum, D.G.; Klein, M. *Survival Analysis: A Self-Learning Text*, 3rd ed.; Springer: New York, NY, USA, 2012.
24. Franco, M.N.; Sánchez, J.; De Miguel, C.; Martínez, M.; Martín-Vertedor, D. Influence of the Fruit's Ripeness on Virgin Olive Oil Quality. *J. Oleo Sci.* **2015**, *64*, 263–273. [CrossRef] [PubMed]